


## Influence of crystalline order and defects on the absolute work functions and electron affinities of TiO<sub>2</sub>- and SrO-terminated *n*-SrTiO<sub>3</sub>(001)

Scott A. Chambers and Peter V. Sushko

*Physical and Computational Sciences Directorate, Pacific Northwest National Laboratory Richland, Washington 99352, USA*

 (Received 9 October 2019; published 23 December 2019)

We explore how the structure and composition of the terminal layer of *n*-SrTiO<sub>3</sub>(001) determine key surface electronic properties. We have measured and calculated from first principles the absolute work functions and electron affinities of bulk SrNb<sub>0.01</sub>Ti<sub>0.99</sub>O<sub>3</sub>(001) terminated along the TiO<sub>2</sub> and SrO planes. The match between theory and experiment is quite satisfactory for the TiO<sub>2</sub> termination if an ideal, bulk-truncated surface structure is assumed. In contrast, the ideal SrO termination leads to a calculated work function considerably lower than the experimental value. We show that this discrepancy can be associated with defects on the SrO surface that act as electron scavengers. These defects deplete the concentration of itinerant electrons in the subsurface region and increase the negative charge density on the surface, thus increasing the work function. Several different surface defect configurations were modeled; the ones that yield the best agreement with experiment involve Sr vacancies in the terminal layer along with O<sup>2-</sup>, OH<sup>-</sup>/H<sup>-</sup> pairs or O<sub>2</sub><sup>2-</sup> occupying anion sites adjacent to the Sr vacancies.

DOI: [10.1103/PhysRevMaterials.3.125803](https://doi.org/10.1103/PhysRevMaterials.3.125803)

### I. INTRODUCTION

Complex oxide surfaces are of considerable current interest for both fundamental materials physics research [1–4] and applications ranging from solid-state device technology [5] to electrocatalysis and photoelectrochemistry [6]. The energy required to liberate electrons from a surface, i.e., the work function ( $\Phi$ ), is a basic surface property that has been accurately measured for many pure metals and elemental semiconductors, such as Si and Ge [7]. Likewise, the electron affinity ( $\chi$ ) is a fundamental property governing the ease with which electrons can be captured by a surface and has been measured for several elemental materials. Both  $\Phi$  and  $\chi$  are sensitive to the composition and structure of the surface. As a result, these quantities are harder to definitively establish for complex materials, such as metal oxides, because of the large number of structural and compositional degrees of freedom [8]. Additionally, the interfacial environment of the surface (i.e., whether the surface is in ultrahigh vacuum or exposed to a gas or solution ambient) can have a substantial effect on the measured values of  $\Phi$  and  $\chi$  through adsorption of molecular species.

For any material of interest,  $\Phi$  and  $\chi$  for its free surfaces in a clean, ultrahigh vacuum environment constitute an important baseline and should be accurately established as part of determining these quantities and understanding their behavior in electronic devices and energy capture and conversion processes [9]. SrNb<sub>*x*</sub>Ti<sub>1-*x*</sub>O<sub>3</sub>(001), or Nb:STO, is the prototypical complex *n*-type oxide semiconductor used extensively in materials physics investigations, including exploring various device concepts. Nb:STO is readily obtained as a bulk single crystal and is frequently used not only as a substrate on which heterojunctions are deposited, but also as an active layer in heterostructures [10–13]. Additionally, epitaxial films of *n*-SrTiO<sub>3</sub>(001) doped with Nb<sub>Ti</sub>, La<sub>Sr</sub>, or V<sub>O</sub> have been

utilized in a variety of heterostructures, with impressively high low-temperature electron mobilities in some cases [14]. Yet, despite decades of research on this material, there is no consensus regarding  $\Phi$  and  $\chi$  values, precluding efforts to predictively design and fabricate reliable functional systems involving free STO(001) surfaces. A range of  $\Phi$  values appear in the literature. For example, Susaki *et al.* [15–17] report values from 4.0 to 4.8 eV for TiO<sub>2</sub>-terminated Nb:STO(001) surfaces prepared in nominally the same way, and from 2.5 to 3.0 eV for SrO-terminated surfaces of homoepitaxial films of undoped STO deposited on Nb:STO(001) substrates using pulsed laser deposition (PLD). These data were taken with a macroscopic Kelvin probe in a measurement chamber appended to the PLD system. This tool measures  $\Phi$  values relative to that of a stainless-steel counterelectrode which is, in turn, calibrated against an electrode with an *in situ* deposited Au film, assuming the latter to have a  $\Phi$  value of 5.1 eV. The wide range of values reported for TiO<sub>2</sub>-terminated Nb:STO(001) was ascribed to different vacuum conditions for the two sets of measurement, implying that the surfaces may not have been clean [15,16]. Missing from the analysis of  $\Phi$  and  $\chi$  is discussion of the dependence of these properties on the presence of surface defects. Even though a conceivable role for surface defects is widely acknowledged and significant deviations of surface structures from ideal terminations are directly observed [18], the atomistic structures of these defects and relationships to STO electronic properties remain elusive.

Quantifying  $\Phi$  and  $\chi$  is necessary to establish a reference for such a widely used material. To this end, we have used angle-integrated ultraviolet photoelectron spectroscopy (UPS) to determine absolute values of  $\Phi$  and  $\chi$  for clean surfaces of bulk Nb:SrTiO<sub>3</sub>(001) crystals with the two surface terminations, as well as for oxygen-vacancy-doped (V<sub>O</sub>) *n*-SrTiO<sub>3- $\delta$</sub>  epitaxial films grown on *p*-Ge(001). We also address

the influence of band bending on  $\Phi$  and  $\chi$  by measuring these three properties simultaneously using UPS in conjunction with x-ray photoelectron spectroscopy (XPS). The methodology presented here is readily transferable to other semi-conducting surfaces. We have also carried out first-principles calculations of the work functions for the two terminations of STO(001) with a range of surface structures in order to link the measured values to the details of the surface termination.

## II. EXPERIMENTAL AND MODELING DETAILS

Bulk  $\text{SrNb}_{0.01}\text{Ti}_{0.99}\text{O}_3(001)$  crystals from CrysTec GmbH were prepared by sonication in acetone and isopropanol, etching in buffered HF for 30 s, and rinsing in deionized (DI) water followed by isopropyl alcohol. The wafers were annealed for 4 h at 1000 °C in an air-filled tube furnace, with 4-hr ramp-up and ramp-down times, and then rinsed again in DI water. This process results in a reasonably well-defined  $\text{TiO}_2$ -terminated surface with a terrace-step structure commensurate with the vendor-specified crystal miscut ( $\leq \sim 0.1^\circ$ ) [19]. Once under vacuum, the surfaces were cleaned by annealing in an electron cyclotron resonance oxygen plasma beam with an oxygen background pressure of  $1.5 \times 10^{-6}$  Torr for 30 min at a temperature of 600 °C. We have found this cleaning procedure to consistently and reliably remove adventitious carbon from the surfaces of several different oxide single crystals, including (but not limited to)  $\text{SrTiO}_3(001)$ ,  $\text{MgAl}_2\text{O}_4(001)$ ,  $\text{MgO}(001)$  and  $\alpha\text{-Al}_2\text{O}_3(0001)$ , to levels below the XPS detection limit ( $\sim 0.1\%$ ). SrO-terminated surfaces were prepared by depositing 1.0 monolayer of SrO by plasma-assisted molecular-beam epitaxy (MBE) on  $\text{TiO}_2$ -terminated surfaces at a temperature of 600–650 °C. Epitaxial films of  $V_{\text{O}}$ -doped  $n\text{-SrTiO}_3(001)$  were deposited on  $p\text{-Ge}(001)$  by MBE as described elsewhere [20].

UPS and XPS measurements were carried out at ambient temperature in an analytical chamber appended to the MBE system equipped with an Omicron/Scienta R3000 analyzer having a  $30^\circ$  acceptance cone. Monochromatic He I vacuum ultraviolet (VUV) photons ( $h\nu = 21.2$  eV) were used for UPS and monochromatic  $\text{AlK}\alpha$  x rays ( $h\nu = 1487$  eV) were used for XPS. The energy resolution was  $\sim 60$  meV in UPS and  $\sim 400$  meV in XPS. The spectrometer resolution and absolute binding energy scales were determined using the Fermi level and the  $3d_{5/2}$  core level for a clean, polycrystalline Ag foil. UPS valence-band (VB) spectra were collected with the sample biased to  $-10$  V in order to accelerate photoelectrons near the zero-kinetic-energy cutoff by  $+10$  eV, thus minimizing their loss from the signal due to stray magnetic fields, and insuring that the sample rather than the analyzer work function is measured.

In order to relate the observed dependence of the work function on surface termination to the atomistic structure of STO(001) surfaces, we represented both terminations using periodic slab models and used density-functional theory (DFT) to calculate the corresponding work-function values. Here, we used slabs that have mirror-symmetry  $\text{TiO}_2$  planes at their centers and equivalent atomic structures on both terminating surfaces [Fig. 1(a)]. Unless stated otherwise, the simulations were conducted for slabs containing 17 ( $\text{TiO}_2$  termination) and 19 (SrO termination) atomic planes. We used

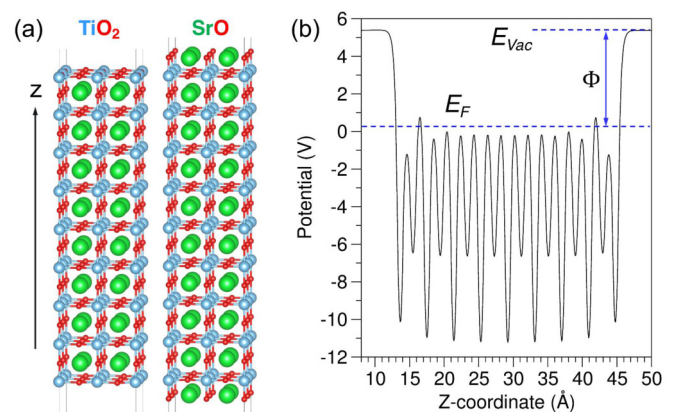


FIG. 1. (a) Periodic slabs with a  $2a_0 \times 2a_0$  lateral cell used to model  $\text{TiO}_2$ - and SrO-terminated surfaces of  $\text{SrTiO}_3(001)$ . (b) Electrostatic potential averaged in the  $x$ - $y$  plane and plotted as a function of slab  $z$  coordinate. The work function  $\Phi$  is defined by the difference between the potential energy in the vacuum gap ( $E_{\text{vac}}$ ) and the Fermi energy ( $E_{\text{F}}$ ) in the slab.

a  $2a_0 \times 2a_0$  lateral cell, where the lateral lattice parameter  $a_0$  was fixed at the experimental value of 3.905 Å; the off-plane parameter was fixed at 50 Å, which leaves a vacuum gap of over  $\sim 15$  Å for all considered systems. The work function was defined as the difference between the Fermi energy of the slab and the electrostatic potential in the vacuum gap of the supercell [see Fig. 1(b)]. In turn, the Fermi energy was tied to the energy of the highest occupied one-electron state at the bottom of the conduction band (CB). To this end, the slab was  $n$  doped and the amount of the excess electron charge ( $N_e$ ) at the bottom of the CB was varied from  $1e^-$  to  $0.001e^-$  per supercell. This excess electron charge was compensated using a homogeneous positively charged background. The work-function values were calculated as functions of the electron charge in the CB for the ideal and several defect-containing slab surfaces. We note that this approach creates an artificial electric field due to excess positive charge in the vacuum gap and excess negative charge inside the slab. Therefore, at large values of  $N_e$ , the calculated work-function values are artificially low due to the electric field generated by this charge distribution. However, as the magnitude of  $N_e$  is scaled downward, this artificial field becomes small and eventually negligible.

The simulations were conducted using the Vienna *Ab initio* Simulation Package (VASP) [21,22]. The projector-augmented wave potentials were used to approximate the effect of the core electrons [23]. In all cases, we used the Perdew-Burke-Ernzerhof generalized gradient approximation developed for solids (PBEsol) density functional [24]. Internal degrees of freedom were fully relaxed. A gamma-centered  $k$  mesh was used for Brillouin-zone integration:  $2 \times 2 \times 1$  mesh was used for the structure optimizations and  $4 \times 4 \times 1$  for subsequent single-point energy calculations. One-electron densities of states (DOS) were calculated using a  $12 \times 12 \times 1$   $k$  mesh. The Hubbard  $U_{\text{eff}}$  correction ( $U_{\text{eff}} = U - J$ ) was applied to Ti  $3d$  states in selected cases [24]. The plane-wave basis-set cutoff was set to 500 eV. The  $n$ -type character for the STO slab was simulated using either two oxygen vacancies ( $V_{\text{O}}$ ) or substitutional Nb dopants on Ti sites ( $\text{Nb}_{\text{Ti}}$ ) distributed in the inner part of the slab.

### III. RESULTS

#### A. Surface stoichiometry

In order to accurately establish the STO(001) surface termination, we used Ti 2*p* and Sr 3*d* core-level XPS intensities measured at normal emission and interpreted using a simple model. For a 100% TiO<sub>2</sub>-terminated *n*-STO(001) surface, the Ti 2*p* intensity can be expressed as

$$I_{\text{Ti}2p}(\theta) = AI_0 \left( \frac{d\sigma_{\text{Ti}2p}}{d\Omega} \right) T(E_k, \theta) \sum_{i=0}^n \exp\left(-\frac{ic}{\lambda_{\text{Ti}2p} \cos\theta}\right). \quad (1)$$

Here,  $I_0$  is the total incident x-ray intensity (photons/s),  $A$  is the area defining the analyzer field of view,  $\left(\frac{d\sigma_{\text{Ti}2p}}{d\Omega}\right)$  is the differential photoionization cross section,  $T(E_k, \theta)$  is the spectrometer transmission function,  $\lambda_{\text{Ti}2p}$  is the electron attenuation depth,  $\theta$  is the emission angle relative to the surface normal, and  $c$  is the out-of-plane lattice parameter for STO. The analogous expression for the Sr 3*d* intensity from the same surface is

$$I_{\text{Sr}3d}(\theta) = AI_0 \left( \frac{d\sigma_{\text{Sr}3d}}{d\Omega} \right) T(E_k, \theta) \sum_{i=0}^n \exp\left[-\frac{(i+0.5)c}{\lambda_{\text{Sr}3d} \cos\theta}\right]. \quad (2)$$

X-ray photoelectron diffraction (XPD) effects [25] have been neglected in writing down these formulae. XPD measurements within a cone of emission centered at the surface normal for STO(001) shows that both Sr 3*d* and Ti 2*p* intensities peak along [001] due to the well-known forward focusing effect [25–28], resulting in comparable intensity enhancements for both core levels. If the surface is SrO terminated with 100% occupancy of all Sr sites in the top layer, the arguments of the exponential terms in the sums over layers can be exchanged in Eqs. (1) and (2). If, however, there are Sr vacancies in the terminal SrO layer, as our experimental and theoretical work-function results suggest (discussed in Secs. III B and III C), then Eq. (2) must be modified to read

$$I_{\text{Sr}3d}(\theta) = AI_0 \left( \frac{d\sigma_{\text{Sr}3d}}{d\Omega} \right) T(E_k, \theta) \sum_{i=0}^n p_i \exp\left(-\frac{ic}{\lambda_{\text{Sr}3d} \cos\theta}\right), \quad (3)$$

where  $p_i$  is the fractional Sr occupancy of the  $i$ th SrO layer,  $i = 0$  being the terminal layer. If Sr vacancies are present only in the top layer,  $p_0 < 1$  and  $p_i = 1$  for all  $i > 0$ . In this case, Eq. (3) can be combined with

$$I_{\text{Ti}2p}(\theta) = AI_0 \left( \frac{d\sigma_{\text{Ti}2p}}{d\Omega} \right) T(E_k, \theta) \sum_{i=0}^n \exp\left[-\frac{(i+0.5)c}{\lambda_{\text{Ti}2p} \cos\theta}\right] \quad (4)$$

to simulate the core-level XPS intensities for SrO-terminated *n*-STO(001).

The lack of accurate, material-specific differential photoelectric cross-sections values for Ti 2*p* and Sr 3*d* in Nb:STO(001), along with inadequately characterized transmission functions, render Eqs. (1)–(4) of semiquantitative value when predicting intensities and intensity ratios for a given surface termination. (See, for example, the stark differences

in the Ti 2*p* line shapes for single crystals of STO(001) in Ref. [29] and Ti<sub>2</sub>O<sub>3</sub> in Ref. [30], none of which are predicted by calculated free-atom cross sections such as those found in Ref. [31].) To mitigate this problem, we used the ratio of the Ti 2*p*-to-Sr 3*d* peak area ratios for the two terminations, denoted as  $\mathcal{R}$ , as calculated using Eqs. (1)–(4) and compared to experiment.

$$\mathcal{R} = \frac{[I_{\text{Ti}2p}(\theta)/I_{\text{Sr}3d}(\theta)]_{\text{TiO}_2 \text{ term}}}{[I_{\text{Ti}2p}(\theta)/I_{\text{Sr}3d}(\theta)]_{\text{SrO term}}}. \quad (5)$$

Using this approach, all prefactors cancel out, leaving only ratios of sums over layers, which in turn depend on electron attenuation lengths and atom distributions as a function of depth. The average Ti 2*p*<sub>3/2</sub>-to-Sr 3*d* peak area ratio measured at normal emission ( $\theta = 0^\circ$ ) with AlK $\alpha$  x rays after annealing several as-prepared TiO<sub>2</sub>-terminated crystals in activated oxygen is 0.674(5). The same ratio after deposition of 1.0 ML SrO averaged over multiple samples is 0.565(1), yielding an  $\mathcal{R}$  value of 1.19(1). The  $\mathcal{R}$  value calculated using Eqs. (1) and (2) with  $\lambda$  values of 20 and 17 Å for Sr 3*d* and Ti 2*p*, respectively [32], is 1.24, in excess of the experimental value. To account for this disagreement, we consider the possibility of Sr vacancies on the SrO-terminated surface, as suggested by our theoretical modeling of the work function (see Sec. III C). Using Eqs. (1)–(4) with  $p_0 = 0.75$  (25% Sr vacancies) leads to an  $\mathcal{R}$  value of 1.18, in excellent agreement with experiment. If the TiO<sub>2</sub>-terminated surface consists of two monolayers of TiO<sub>2</sub> as suggested elsewhere [33], the corresponding  $\mathcal{R}$  values calculated using Eqs. (1)–(4) with  $p_0 = 0.75$  and 1.00 would be 1.45 and 1.52, respectively, which are both considerably larger than the experimental value.

#### B. Work function and electron affinity measurements

A schematic energy diagram illustrating how we used UPS to determine both  $\Phi$  and  $\chi$  for SrNb<sub>0.01</sub>Ti<sub>0.99</sub>O<sub>3</sub>(001) (a degenerately doped *n*-type semiconductor) with some band bending  $\delta V$  is shown in Fig. 2. ( $\delta V \equiv E_V - E_g$ , where  $E_V$  is the valence-band maximum at the surface and  $E_g$  is the bulk band gap.) The photon energy is represented by the length of the red arrows marked  $h\nu$  in the center of the figure. Photoelectrons from the occupied states (indicated as VB DOS in the lower right) produce the three-peak spectrum seen in the upper right. This spectrum consists of the instrumentally and vibrationally broadened valence-band density of states (VB DOS) modulated by photoelectric cross sections for the different elemental and orbital contributions to the VB (shaded blue). Also visible is a broad band at higher binding energy that cuts off at zero kinetic energy,  $E_k^0$  (shaded red). This band consists of inelastically scattered VB electrons. The two red arrows represent photoelectrons excited from the Fermi level ( $E_b = 0$ , left), and from the low-energy cutoff ( $E_k = 0$ , right). The position of the low-energy cutoff is determined by the vacuum level ( $E_{\text{vac}}$ ), which is defined as the energy of a free electron at rest within a few nanometers of the surface [7]. The blue double-ended arrow labeled  $\Delta E$  is the energy difference between the Fermi level and the low-energy cutoff in the measured spectrum. By inspection, the work function,  $\Phi$ , is given by  $\Phi = h\nu - \Delta E$ , and the electron



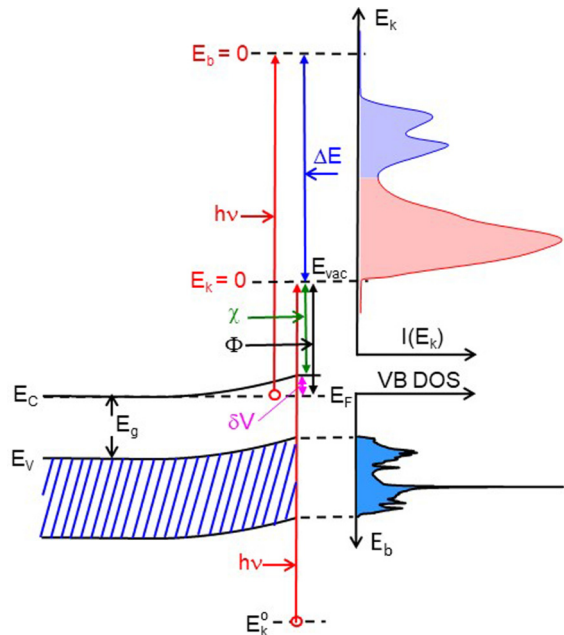


FIG. 2. Energy diagram for ultraviolet photoemission from an  $n$ -type semiconductor with some upward band bending indicating how the work function ( $\Phi$ ) and the electron affinity ( $\chi$ ) can be measured.

affinity by  $\chi = \Phi + \delta V$  ( $\delta V$  is negative for upward band bending). For a degenerately doped  $n$ -type semiconductor, the electron affinity is numerically equal to the work function if there is no band bending ( $\delta V = 0$ ).

For lightly doped semiconductors, the entire UPS spectrum can shift if the positive charge caused by photoemission from the intense He I beam is not fully compensated by electrons from ground. Moreover, surface photovoltage (SPV) effects can occur at any dopant concentration, also precluding accurate measurement of  $\delta V$  [34]. In order to detect these artifactual spectral shifts, the energy distribution of the He I-excited VB was compared with that measured using AlK $\alpha$  x rays by overlaying the two spectra and checking for good overlap along the leading edge. The much lower x-ray flux results in negligible static charging and SPV, thereby generating an internal standard for the VUV spectrum.

UPS spectra for what our modeling (Sec. III C) indicates is a nearly defect-free TiO<sub>2</sub>-terminated Nb:STO(001) surface, as cleaned by heating in activated oxygen in the appended MBE chamber and after 15-min anneals in ultrahigh vacuum at the indicated temperatures, are shown in Fig. 3(a). The corresponding AlK $\alpha$ -excited Ti 2p<sub>3/2</sub> spectra are shown in Fig. 3(b). The Ti 2p<sub>3/2</sub> line shapes reveal that the UHV annealing does not result in any measurable V<sub>O</sub> creation in the Nb:STO lattice. Itinerant electrons from V<sub>O</sub> would screen structural Ti<sup>4+</sup> cations, giving rise to the apparent presence of Ti<sup>3+</sup> since the bottom of the STO conduction band is Ti 3d derived. This phenomenon would in turn produce a weak feature in the Ti 2p<sub>3/2</sub> spectrum shifted  $\sim 2$  eV to lower binding energy. However, no such feature is seen. Some Ti<sup>3+</sup> is also expected due to screening of B-site Ti<sup>4+</sup> cations by itinerant electrons from Nb dopants [35]. However, no detectable Ti<sup>3+</sup> feature was observed at 1 at %, the Nb concentration, most likely because of the presence of deep-gap trap states in STO

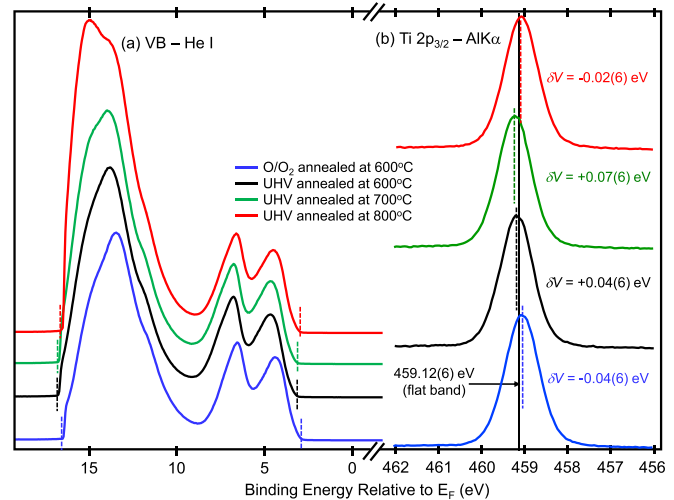


FIG. 3. (a) Valence-band photoemission spectra excited with He I vuv light, and (b) Ti 2p<sub>3/2</sub> core-level spectra excited with AlK $\alpha$  x rays for bulk TiO<sub>2</sub>-terminated SrNb<sub>0.1</sub>Ti<sub>0.99</sub>O<sub>3</sub>(001) as cleaned by annealing in activated oxygen, and after anneals in ultrahigh vacuum at temperatures ranging from 600 to 800 °C.

associated with interstitial O that are not of Ti 3d character [36]. The band bending can be accurately determined from the Ti 2p<sub>3/2</sub> and Sr 3d<sub>5/2</sub> binding energies using the expression

$$\delta V = 0.5\{[E_{\text{Ti}2p_{3/2}} - (E_{\text{Ti}2p_{3/2}} - E_{\text{v}})_{\text{ref}}] + [E_{\text{Sr}3d_{5/2}} - (E_{\text{Sr}3d_{5/2}} - E_{\text{v}})_{\text{ref}}]\} - E_{\text{g}}. \quad (6)$$

Here we use measured differences between the Ti 2p<sub>3/2</sub> and Sr 3d<sub>5/2</sub> binding energies and the VB maximum for a reference surface of clean  $n$ -SrTiO<sub>3</sub>(001) to determine the VB maximum relative to the Fermi level averaged over the two core levels for the surface of interest. We then subtract the STO band gap from this quantity to obtain  $\delta V$ . Our sign convention is that  $\delta V$  is positive for downward band bending and negative for upward band bending. The resulting values of  $\delta V$  are shown adjacent to the Ti 2p<sub>3/2</sub> spectra in Fig. 3(b). The UHV anneals result in slight changes in  $\delta V$ , modulating from upward band bending as cleaned to downward band bending after anneals at 600 and 700 °C, followed by a very nearly flat-band state after the 800 °C anneal. Similarly, the UPS VB spectra rigidly shift to slightly higher binding energy relative to the as-cleaned surface, indicating slight downward band bending after the anneals at 600 and 700 °C, to near flat band after annealing at 800 °C. These trends are indicated by the vertical dashed lines that show the energies at which the count rates go to zero on both ends of each spectrum. Inspection of these data reveals that the total spectral width is invariant with respect to slight changes in band bending, indicating that the vacuum level is pinned to the band edge for this surface. This result suggests that for near-defect-free TiO<sub>2</sub>-terminated  $n$ -STO(001), the surface charge that causes the band bending also modulates the work function. In contrast, the band bending was found to be much smaller than the change in work function for  $n$ -ZnO(0001) and (000 $\bar{1}$ ) [8].

In order to determine  $\Phi$  for the two bulk terminations, the trailing edge of the low-energy cutoff ( $E_{\text{k}}^0$ ) was extrapolated to the energy axis for each He I-excited spectrum, examples of which are seen in Figs. 4(a) and 4(b). Good overlap with

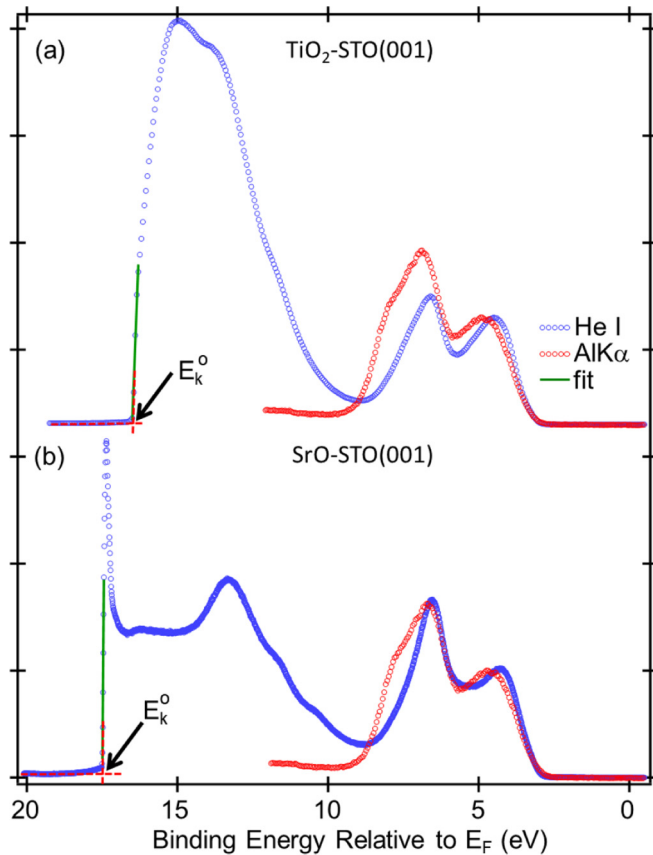


FIG. 4. He I valence-band spectra for (a) TiO<sub>2</sub>- and (b) SrO-terminated SrNb<sub>0.1</sub>Ti<sub>0.99</sub>O<sub>3</sub>(001) from which the low-energy cutoffs ( $E_k^o$ ) were measured to determine the work function. A reference AlK $\alpha$ -excited spectrum, positioned according to the Ti  $2p_{3/2}$  and Sr  $3d_{5/2}$  core-level binding energies for the specific sample, is overlaid to detect the presence of charging or surface photovoltage effects in UPS. The spectrum in (a) is the one measured after the 800 °C anneal (see Fig. 3).

the AlK $\alpha$ -excited spectra along the leading edge shows that charging is negligible in the UPS spectra. The resulting  $\Phi$  values, given by  $h\nu - E_k^o$ , are shown in Table I, along with the corresponding  $\delta V$  values from core-level binding energies. Table I reveals that the work function is slightly higher after annealing in activated oxygen to remove residual carbon compared to its values after the UHV anneals. The  $\Phi$  values for two SrO-terminated surfaces are both significantly lower than those for the TiO<sub>2</sub>-terminated surfaces. For both terminations, there is some variability in the work function. In the case of the TiO<sub>2</sub>-terminated surface, the variation is tied to the amount of band bending, as can be seen by comparing the electron affinities, shown in the last column of Table I. The difference in work function for our two terminations is somewhat larger than that of Sokolović *et al.* [18] obtained using a Kelvin probe microscope to measure the work-function difference between patches of TiO<sub>2</sub>- and SrO-terminated STO(001) cleaved in UHV.

We also measure  $\Phi$  for epitaxial  $n$ -SrTiO<sub>3- $\delta$</sub>  (001) films on  $p$ -Ge(001) and compare with results for bulk single crystals. Antiphase boundaries (APBs) form in epitaxial perovskite films grown on Group IV semiconductors due to the sym-

TABLE I. Work functions and electron affinities for several  $n$ -SrTiO<sub>3</sub>(001) surfaces.

	$\delta V$ (eV) <sup>a</sup> ( $\pm 0.06$ )	$E_k^o$ (eV) ( $\pm 0.1$ )	$\Phi$ (eV) <sup>b</sup> ( $\pm 0.1$ )	$\chi$ (eV) <sup>c</sup> ( $\pm 0.1$ )
TiO <sub>2</sub> termination				
600 °C - activated O	-0.04	16.4	4.8	4.7
600 °C UHV	+0.04	16.7	4.5	4.5
700 °C UHV	+0.07	16.7	4.5	4.6
800 °C UHV	-0.02	16.5	4.7	4.7
SrO termination				
As grown - crystal A	-0.21	17.6	3.6	3.4
As grown - crystal B	-0.01	18.1	3.1	3.1
32 u.c. STO/ $p$ -Ge(001)	-0.06	17.7	3.5	3.4

<sup>a</sup> $\delta V = 0.5([E_{\text{Ti}2p_{3/2}} - (E_{\text{Ti}2p_{3/2}} - E_V)_{\text{ref}}] + [E_{\text{Sr}3d_{5/2}} - (E_{\text{Sr}3d_{5/2}} - E_V)_{\text{ref}}] - E_g$ , where  $(E_{\text{Ti}2p_{3/2}} - E_V)_{\text{ref}} = 455.87(4)$  eV and  $(E_{\text{Sr}3d_{5/2}} - E_V)_{\text{ref}} = 130.49(4)$  eV.

<sup>b</sup> $\Phi = h\nu - \Delta E = h\nu - E_k^o$ .

<sup>c</sup> $\chi = h\nu - E_k^o + \delta V$ .

metry mismatch, and we have observed these in our STO films on Ge(001) [20]. In light of the stacking faults resulting from APB formation, the surface is most likely of mixed termination. Figure 5(a) shows the UPS spectrum for 32 u.c. of V<sub>O</sub>-doped SrTiO<sub>3- $\delta$</sub>  on  $p$ -Ge(001), along with a scanning transmission electron micrograph showing an APB in the film [20]. The Ti  $2p_{3/2}$ -to-Sr  $3d_{5/2}$  peak area ratio for the film is 0.630, partway between those measured for TiO<sub>2</sub> (0.675)- and SrO (0.565)-terminated bulk Nb:STO(001) crystals, consistent with the film surface being of mixed termination. However, determination of  $E_k^o$  and  $\delta V$  leads to  $\Phi$  and  $\chi$  values of 3.5(1) and 3.4(1) eV, respectively, close to those of SrO-terminated bulk Nb:STO(001) (crystal A). These results are not inconsistent with the surface being of mixed termination. If both terminations are present, the low-energy cutoff from the SrO portion would extend further to the low binding kinetic energy side than that of the TiO<sub>2</sub> portion. The composite spectrum would thus consist of two overlapping low-energy cutoffs with the former appearing like a “knee” on the latter. To illustrate, we overlap VB spectra for the two bulk terminations with that from the STO/Ge sample in Fig. 5(b), having removed differences in band bending by aligning the VB leading edges. A linear combination (LC) of the spectra for the two bulk crystals using weighting factors of 0.59 and 0.41 derived from XPS analysis (see above) for the TiO<sub>2</sub> and SrO terminations, respectively, is also included. As Fig. 5(b) shows, the spectrum for the SrO termination dominates the region near the low-energy cutoff in the LC and the trailing edge of the LC nicely overlaps that of the actual STO/Ge spectrum. The detailed structure of the inelastically scattered electron tail for STO/Ge is not the same as that averaged over the two bulk-crystal terminations, leading to differences in the region between the low-energy cutoff and the VB proper. However, the trailing edge at the low-kinetic-energy cutoff is quantitatively mimicked.

### C. The calculated effect of surface defects

Figure 6(a) shows the dependence of  $\Phi$  calculated for the TiO<sub>2</sub>- and SrO-terminated slabs on the amount of charge

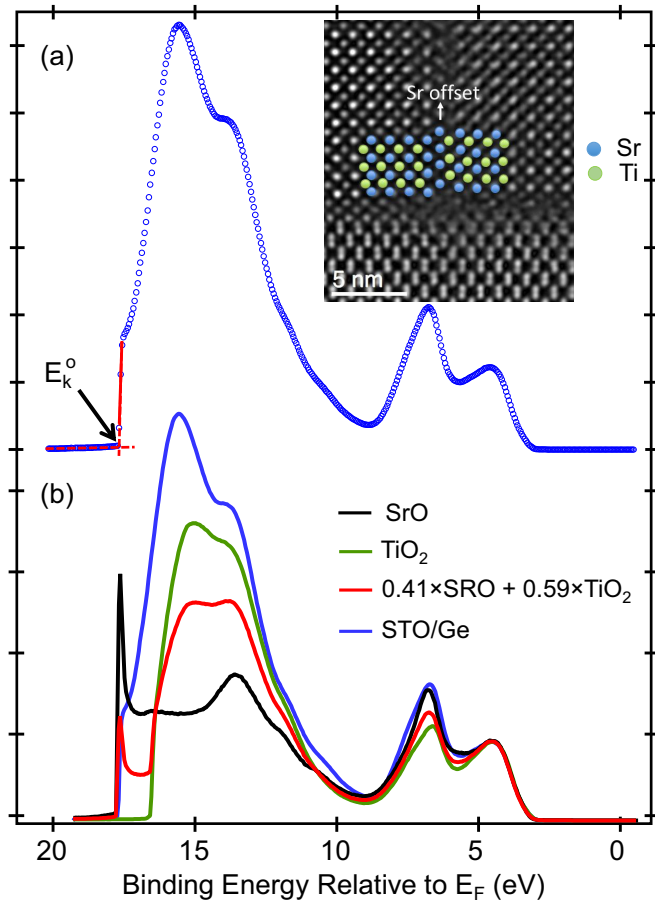


FIG. 5. (a) Valence-band spectrum for 32 u.c. of  $n$ -SrTiO<sub>3-d</sub> on  $p$ -Ge(001). Inset: scanning transmission electron microscopy image of the interface showing a stacking fault in the film associated with an antiphase domain boundary, resulting in both TiO<sub>2</sub>- and SrO terminations on the film surface. (b) Overlay of the spectrum in (a) with a linear combination of spectra for TiO<sub>2</sub>- and SrO-terminated  $n$ -STO(001) showing that a portion of the STO/Ge surface exhibits the same work-function value as SrO-terminated STO.

$N_e$  at the bottom of the CB.  $N_e = 1e^-$  corresponds to an electron concentration of one electron per slab, i.e.,  $\sim 4.7 \times 10^{20} e^-/\text{cm}^3$ , which is a few times larger than the nominal concentration expected by the 1% Nb  $B$ -site doping in the bulk of the STO crystals ( $1.67 \times 10^{20} e^-/\text{cm}^3$ ). We previously reported the existence of deep in-gap trap states in STO which result in the bulk carrier concentration in Nb:STO being  $\sim 30\%$  of the nominal value determined by the Nb dopant concentration [36]. In the near-surface region, the carrier concentration may be lower due to the additional effect of surface traps. Progressively scaling  $N_e$  to lower values allows us to estimate  $\Phi$  across a feasible carrier concentration range and to eliminate the artificial electric-field contribution discussed above. We consider the range  $N_e = 0.001-0.01e^-$  as being a reasonable estimate for the electron density that allows us to probe the position of the CB minimum. The corresponding range of calculated  $\Phi$  values (4.5–4.7 eV) for the TiO<sub>2</sub>-terminated surface overlaps the experimental results shown in Figs. 3 and 4 and agrees with earlier calculations [37].

The situation is quite different for SrO-terminated STO. In the case of an ideal termination,  $N_e = 0.001e^-$  results in a  $\Phi$  value of only  $\sim 2.3$  eV [Fig. 6(a)]. While consistent with previous simulations [37], this value is markedly lower than the experimental values reported here. Our XPS results (see Sec. III A) suggest that the SrO-terminated surface contains a high concentration of Sr vacancies. We considered the effect of these defects by calculating  $\Phi$  for the SrO-terminated surface containing equal quantities of Sr and O surface vacancies. To capture a wide range of vacancy concentrations, we used  $2\sqrt{2}a_0 \times 2\sqrt{2}a_0$  and  $4a_0 \times 4a_0$  lateral cells with the number of atomic planes selected such that the volume of supercell remains approximately the same. The inset in Fig. 6(b) shows the specific arrangement of 50% surface vacancies in the case of the  $2\sqrt{2}a_0 \times 2\sqrt{2}a_0$  cell. Indeed,  $\Phi$  increases with decreasing SrO surface coverage, reaching  $\sim 2.7$  eV (for  $2\sqrt{2}a_0 \times 2\sqrt{2}a_0$  cell) and 2.9 eV (for  $4a_0 \times 4a_0$  cell) for 50% coverage. We associate this effect with exposure of the subsurface TiO<sub>2</sub> planes. In the case of the ideal SrO-terminated surface, the Ti 3d states near the surface are confined by the outermost SrO plane. The effect of this confinement is reduced with increasing SrO vacancy concentration at the surface and, in addition, the electrostatic potential at the exposed Ti sites becomes less negative. Both changes contribute to a shift in Fermi energy to lower values, leading to a larger  $\Phi$ . However, even for 50% SrO coverage, the calculated  $\Phi$  for this surface is lower than the experimental values.

Another factor that can strongly affect  $\Phi$  is the orientation of surface defects formed by Sr and O vacancies. For example, if the Sr vacancy is in the outermost SrO plane and the O vacancy is in the TiO<sub>2</sub> plane immediately below it, the Sr-O vacancy configuration introduces a local dipole in the off-plane direction. This out-of-plane Sr-O vacancy pair results in a  $\Phi$  value of  $\sim 3.3$  eV, which is  $\sim 1$  eV larger than that calculated for (1) the ideal SrO termination, and (2) the same surface with in-plane SrO vacancies. While the off-plane configuration of the  $V_{\text{Sr}} - V_{\text{O}}$  pair is  $\sim 2.6$  eV less stable than the in-plane analog, this finding suggests that surface defects giving rise to dipole moments normal to the surface with their positive charge in the subsurface TiO<sub>2</sub> plane and their negative charge in the terminal SrO plane would produce an electric field that can shift  $\Phi$  upward by several tenths of an electron volt.

To test this hypothesis, we considered several types of defects that would produce such an electric field. As a baseline, we selected the SrO-terminated surface with one-quarter of the neighboring Sr and O atoms in the surface plane missing, giving rise to in-plane Sr-O vacancy pairs (denoted hereafter as  $V_{\text{SrO}}$ ). We found that dissociative chemisorption of a water molecule on  $V_{\text{SrO}}$ , in which the OH<sup>-</sup> occupies a  $V_{\text{O}}$  site and the H<sup>+</sup> binds to a surface O<sup>2-</sup> ion [Fig. 7(a)], has a negligible effect on the work function [compare Fig. 7(e) and Fig. 6(b)]. In contrast, adsorption of an oxygen atom on the O end of a  $V_{\text{SrO}}$  [Fig. 7(b)] shifts the calculated work-function value by  $\sim 0.7$  eV to 2.9–3.1 eV [Fig. 7(e)] depending on whether the CB electrons originate from bulk O vacancies ( $V_{\text{O}}$ ) or Nb<sub>Ti</sub>. This configuration yields good agreement with experiment for crystal B. In both cases, these electrons are trapped by the adsorbed O. The effect is even



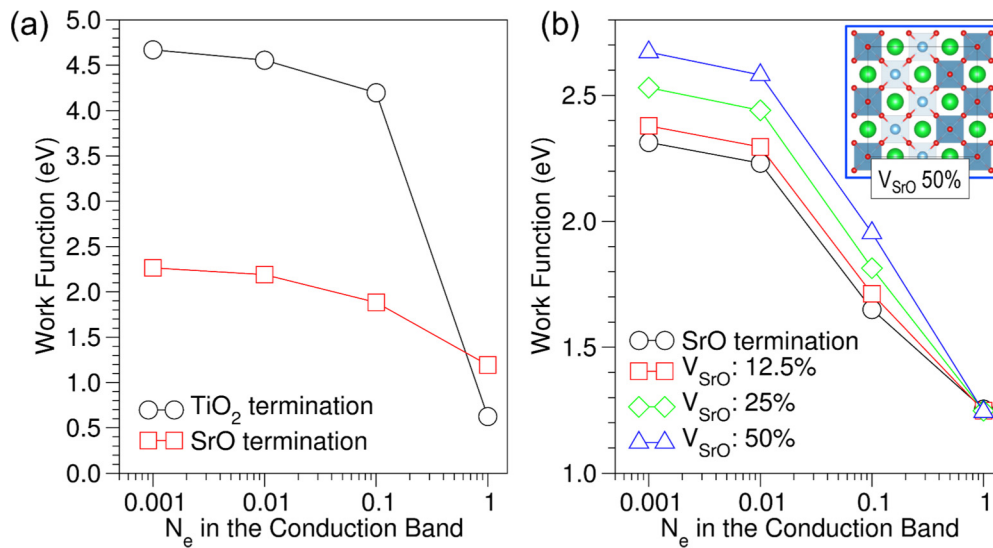


FIG. 6. (a) The dependence of the calculated work function on the concentration of the electrons at the bottom of the CB for the ideal  $\text{TiO}_2$ - and SrO-terminated surfaces. The calculated  $\Phi$  is in good agreement with experiment for the  $\text{TiO}_2$ -terminated surface but is underestimated by  $\sim 1$  eV for the SrO-terminated surface. (b) The work function increases with increasing concentration of surface SrO vacancies. The inset shows the SrO vacancy arrangement for the 50% coverage case in the  $2\sqrt{2}a_0 \times 2\sqrt{2}a_0$  cell.

stronger if the oxygen vacancy site is occupied by an  $\text{O}_2$  molecule [Fig. 7(c)]. This species also traps electrons from  $V_{\text{O}}$  or  $\text{Nb}_{\text{Ti}}$  and becomes  $\text{O}_2^{2-}$ . However, since the center of the electron charge is shifted outward, the effective surface dipole is larger and the work-function shift to 3.7–4.0 eV [Fig. 7(e)] is greater. We note that the energy with which  $\text{O}_2$  is bound to  $V_{\text{O}}$  (3.9–4.1 eV per  $\text{O}_2$  molecule) is similar to that of O (4.2–4.4 eV per  $1/2\text{O}_2$ ). However, the former does not require overcoming the dissociation barrier and is therefore likely to dominate at room temperature. Finally, we find that in regions with higher  $V_{\text{SrO}}$  concentrations, water

molecules can dissociate with the formation of an  $\text{OH}^-$  and  $\text{H}^+$  ions occupying two surface O vacancy sites [Fig. 7(d)]; the calculated binding energy is 3.8 eV per  $\text{H}_2\text{O}$  molecule. The work function calculated for this case [3.6–3.7 eV, as seen in Fig. 7(e)] is in good agreement with experiment for crystal A. We note that similar work-function values were obtained for this configuration by representing  $n$ -STO using either bulk  $V_{\text{O}}$  or  $\text{Nb}_{\text{Ti}}$ . Based on agreement between theory and experiment for the work function, we conclude that the configurations shown in Figs. 7(b)–7(d) are the most likely to be present on the SrO-terminated surface.

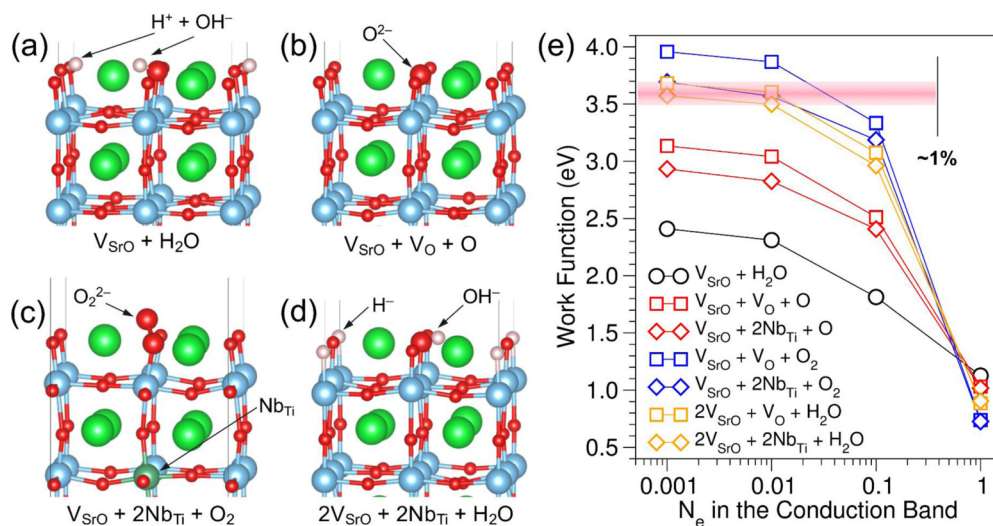


FIG. 7. Configurations of defects formed by surface SrO vacancies interacting with (a)  $\text{H}_2\text{O}$ , (b)  $1/2\text{O}_2$ , (c)  $\text{O}_2$ , and (d)  $\text{H}_2\text{O}$ , resulting in the formation of an  $\text{H}^-/\text{OH}^-$  pair. The  $n$ -type character of STO was simulated using subsurface donors: one  $V_{\text{O}}$  (not seen in the figure) in (b) and (d) and two  $\text{Nb}_{\text{Ti}}$  in (c). (e) Dependence of the calculated work function for the defect-containing SrO-terminated surface on the concentration of the electrons at the bottom of the CB. Configuration notations under images in (a)–(d) correspond to those in the legend in (e). The horizontal pink bar in (e) indicates the maximum possible range of carrier concentrations that could exist for 1 at % Nb-doped STO.

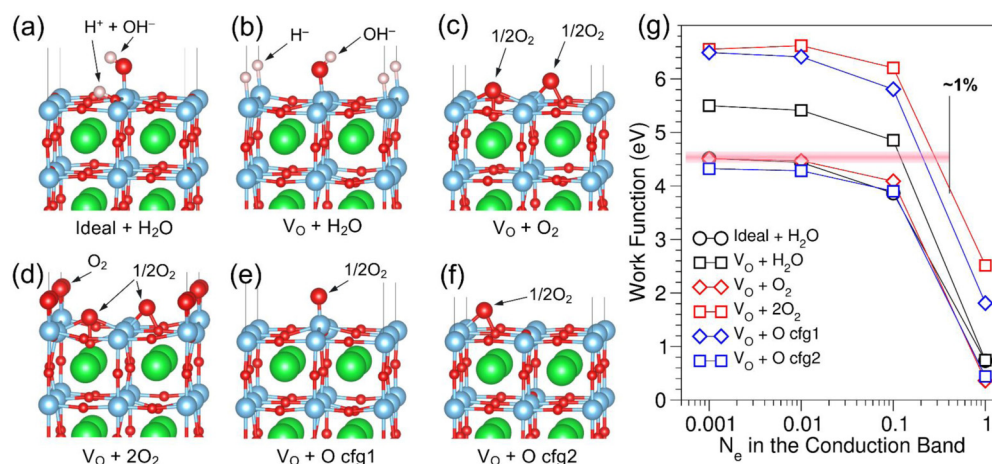


FIG. 8. Configurations of defects formed by the  $\text{TiO}_2$ -terminated surface interacting with (a), (b)  $\text{H}_2\text{O}$  (c), (d)  $\text{O}_2$ ,  $2\text{O}_2$ , and (e), (f)  $1/2\text{O}_2$ . The  $n$ -type character of STO was simulated using  $V_{\text{O}}$  in the subsurface in (b)–(f). (g) The dependence of the calculated work function for the defect-containing  $\text{TiO}_2$ -terminated surface on the electron concentration at the bottom of the CB. Configuration notations under images in (a)–(f) correspond to those in the legend in (g). The horizontal pink bar in (g) indicates the maximum possible range of carrier concentrations that could exist for 1 at % Nb-doped STO.

For completeness, we investigated the effect of the same adsorbed species on the work function of  $\text{TiO}_2$ -terminated  $n$ -STO(001) (see Table II). We did not model the effect of Ti vacancies since we have no evidence that they are present on this surface. The considered defect configurations and the calculated work-function values are shown in Fig. 8. We find that the work function is unaffected by defects that do not trap electrons originating from bulk  $V_{\text{O}}$  or  $\text{Nb}_{\text{Ti}}$ . For example, the work function remains at  $\sim 4.5$  eV after dissociative adsorption of  $\text{H}_2\text{O}$  [Fig. 8(a)] and  $\text{O}_2$  [Fig. 8(c)], leading to the formation of the surface  $\text{H}^+/\text{OH}^-$  pair and two peroxy  $\text{O}_2^{2-}$  species, respectively. The same holds for adsorption of an isolated oxygen atom that forms surface  $\text{O}_2^{2-}$  [Fig. 8(f)]. In contrast, we find that adsorption of electron scavengers increases the work function, as with the SrO termination. For example,  $\text{H}_2\text{O}$  dissociation accompanied by electron trapping

leading to the formation of an  $\text{H}^-/\text{OH}^-$  pair [Fig. 8(b)], nondissociative adsorption of  $\text{O}_2$  leading to the formation of superoxide  $\text{O}_2^-$  [Fig. 8(d)], and adsorption of an oxygen atom at the surface Ti site [Fig. 8(e)] all result in larger work functions. Inasmuch as this effect depends on the surface defect concentration and since the calculated binding energies of adsorbed species to the defects at the  $\text{TiO}_2$ -terminated surface are noticeably smaller than those at the SrO-terminated surface (see Table II), their effect on the work function is small.

It is well known that density functionals based on the generalized gradient density approximation, including PBEsol used in this work, tend to underestimate the one-electron band gap. We tested the robustness of our conclusions by calculating the electronic properties of select defect configurations

TABLE II. Calculated binding energies of adsorbed  $\text{O}_2$  and  $\text{H}_2\text{O}$  on the SrO- and  $\text{TiO}_2$ -terminated surfaces of  $n$ - $\text{SrTiO}_3(001)$  and the corresponding work-function values ( $\Phi$ ) for  $N_e = 0.01e^-$ . See Figs. 7 and 8 for geometrical configurations and the trends in  $\Phi$  with  $N_e$ . Negative binding energies correspond to metastable configurations.  $\text{Nb}_{\text{Ti}}^{5+}$  species are omitted in the second column; each donates one electron to the CB and their formal ionic charge remains 5+ throughout.

SrO termination	Resulting species	Binding energy (eV)	$\Phi$ (eV)
$V_{\text{SrO}} + \text{H}_2\text{O}$	$V_{\text{Sr}} + \text{H}^+ + \text{OH}^-$	2.16	2.31
$V_{\text{SrO}} + V_{\text{O}} + 1/2 \text{O}_2$	$V_{\text{Sr}} + V_{\text{O}}^{++} + \text{O}^{2-}$	4.22	3.04
$V_{\text{SrO}} + 2\text{Nb}_{\text{Ti}} + 1/2 \text{O}_2$	$V_{\text{Sr}} + \text{O}^{2-}$	4.45	2.82
$V_{\text{SrO}} + V_{\text{O}} + \text{O}_2$	$V_{\text{Sr}} + V_{\text{O}}^{++} + \text{O}_2^{2-}$	3.89	3.87
$V_{\text{SrO}} + 2\text{Nb}_{\text{Ti}} + \text{O}_2$	$V_{\text{Sr}} + \text{O}_2^{2-}$	4.14	3.57
$2V_{\text{SrO}} + V_{\text{O}} + \text{H}_2\text{O}$	$2V_{\text{Sr}} + V_{\text{O}}^{++} + \text{H}^- + \text{OH}^-$	1.41–1.71	3.60–3.72
$2V_{\text{SrO}} + 2\text{Nb}_{\text{Ti}} + \text{H}_2\text{O}$	$2V_{\text{Sr}} + \text{H}^- + \text{OH}^-$	3.86	3.50
<b><math>\text{TiO}_2</math> termination</b>	<b>Resulting species</b>	<b>Binding energy (eV)</b>	<b><math>\Phi</math> (eV)</b>
$\text{H}_2\text{O}$	$\text{H}^+ + \text{OH}^-$	1.16	4.44
$V_{\text{O}} + \text{H}_2\text{O}$	$V_{\text{O}}^{++} + \text{H}^- + \text{OH}^-$	-0.67	5.41
$V_{\text{O}} + \text{O}_2 + 2\text{O}_{\text{surf}}^{2-}$	$V_{\text{O}} + 2\text{O}_2^{2-}$	-0.76	4.47
$[V_{\text{O}} + \text{O}_2 + 2\text{O}_{\text{surf}}^{2-}] + \text{O}_2$	$V_{\text{O}}^{+} + 2\text{O}_2^{2-} + \text{O}_2^-$	1.23	6.62
$V_{\text{O}} + 1/2 \text{O}_2\text{cfg1}$	$V_{\text{O}}^{++} + \text{O}^{2-}$	1.46	6.41
$V_{\text{O}} + 1/2 \text{O}_2\text{cfg2} + \text{O}_{\text{surf}}^{2-}$	$V_{\text{O}} + \text{O}_2^{2-}$	-0.26	4.28



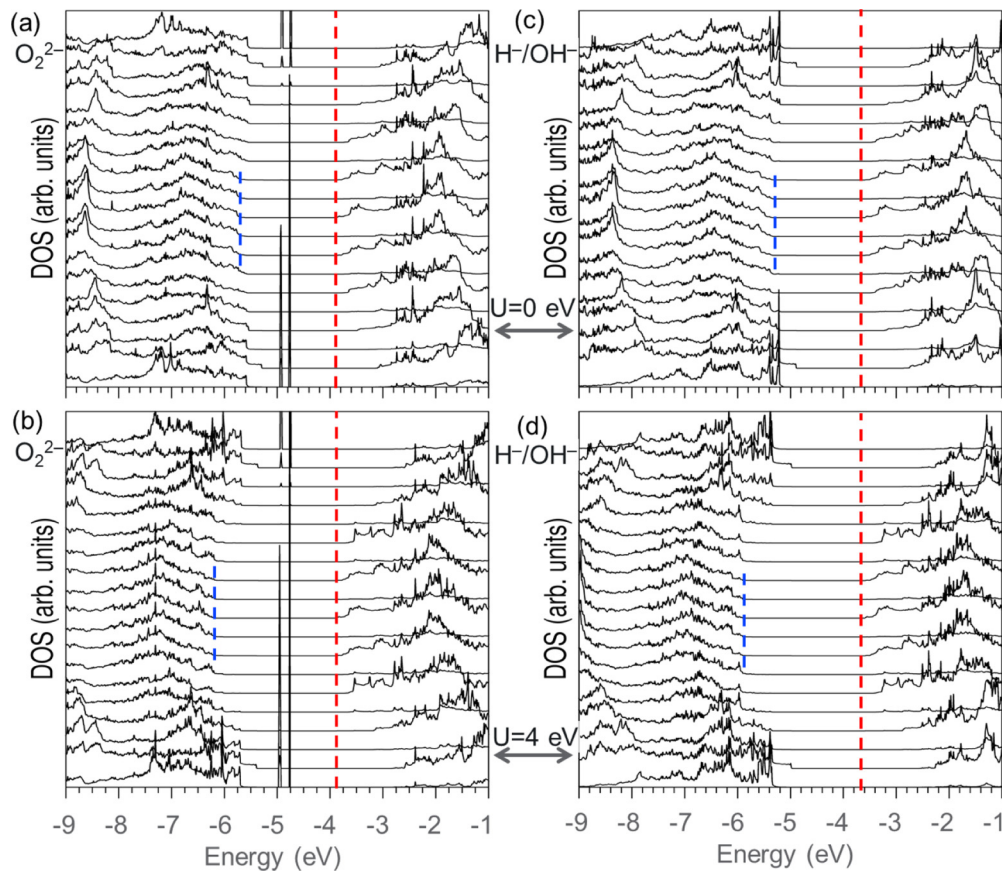


FIG. 9. Layer-projected densities of states (DOS) for the SrO-terminated slabs containing surface electron trap defects, calculated as a function of  $U_{\text{eff}}$ : (a), (b)  $V_{\text{SrO}}(\text{surface}) + V_{\text{O}^{++}}(\text{bulk}) + \text{O}_2^{2-}(\text{surface})$ ; (c), (d)  $2V_{\text{SrO}}(\text{surface}) + V_{\text{O}^{++}}(\text{bulk}) + \text{H}^-(\text{surface}) + \text{OH}^-(\text{surface})$ . The DOS in the  $\text{TiO}_2$  planes were scaled by a factor of 0.5. Zero on the energy scales corresponds to the average electrostatic potential in the vacuum gap. The positions of the CB minimum and VB maximum in the central part of the slab are indicated with red and blue dashed lines, respectively. The Fermi level is at the bottom of the conduction band. As the value of  $U_{\text{eff}}$  increases from 0 eV (a), (c) to 4 eV (b), (d), the band gap increases as well but the work function remains unchanged. Similar behavior was found for  $U_{\text{eff}}$  up to 8 eV.

using the Hubbard  $U_{\text{eff}}$  correction as defined in Ref. [24]. Figure 9 shows the one-electron DOS for SrO-terminated STO(001), projected onto atomic planes for the two surface defect configurations shown in Figs. 7(c) and 7(d) for  $U_{\text{eff}} = 0.0$  and 4.0 eV. In both cases, bulk  $V_{\text{O}}$  was used to mimic  $n$ -type STO and an additional charge of  $N_e = 0.001e$  was provided to occupy the states at the CB minimum. The DOS were aligned such that the average electrostatic potential in the vacuum gap (see Fig. 1) is at zero energy. We find that the band gap increases with the value of  $U_{\text{eff}}$  up to 8 eV. However, the energy of the CB minimum and, therefore, the work function and electron affinity, remain essentially unchanged.

#### IV. DISCUSSION

Both XPS core-level intensities and UPS work-function results, interpreted by *ab initio* calculations, point to the SrO-terminated surface as being highly defective. Theoretical modeling suggests that Sr-O vacancy pairs form on the surface, and that the anion sites are occupied with  $\text{OH}^-/\text{H}^-$  pairs or  $\text{O}_2^{2-}$ . The driver behind Sr vacancy formation on this surface is not known at present. A Sr sticking coefficient of less than unity at our 600 to 650 °C growth temperature range is not a likely explanation since shuttered MBE growth of

stoichiometric, homoepitaxial STO in which monolayer doses of Sr and Ti were incident on the substrate in alternating, sequential order has been reported for temperatures ranging between 550 and 750 °C [38].

Having established the effect of several prototype electron traps on the work function and electron affinity, we propose that the distribution of the measured work-function values reported earlier [15–17] may stem not exclusively from surface contamination, but also from variations in the density and orientation of surface and near-surface defects which impact the magnitude and the direction of the electric field at these surfaces. In turn, the kinds and quantities of these surface electron traps are tied to the nominal dopant concentration, effective carrier concentration [36], and sample processing conditions. For example, measurements for five separate Nb:STO crystals, all prepared the same way to yield a nominal  $\text{TiO}_2$  termination, resulted in electron affinities ranging from 4.7 to 3.9 eV. Moreover, these electron affinities scaled with the Ti 2p-to-Sr 3d XPS peak area ratio. This result suggests that some residual SrO may have been present on the  $\text{TiO}_2$  terraces of samples exhibiting the lower electron affinities. Indeed, one set of first-principles calculations (not shown) predicts that the electron affinity drops from its clean  $\text{TiO}_2$  terminal layer value to 3.9 eV for a SrO coverage

of 0.12 monolayer. As an outlook, we propose that more fully elucidating the complex relationships between work function/electron affinity and surface structure/composition of important complex oxides, leading to the development of the processing approaches that ensure reproducibility of the electronic properties, remains a worthy scientific goal.

## V. SUMMARY

Absolute work functions and electron affinities were measured by means of *in situ* ultraviolet photoelectron spectroscopy for clean TiO<sub>2</sub>- and SrO-terminated Nb:SrTiO<sub>3</sub>(001). The data reveal that for the TiO<sub>2</sub>-terminated surface, the vacuum level shifts in energy with band bending as the surface is annealed in UHV, suggesting that the vacuum level is pinned to the band edge. The SrO-terminated surface exhibits a markedly lower work function relative to that for the TiO<sub>2</sub>-terminated surface, and the change in work function far exceeds the change in band bending. These results indicate that the charge distribution is qualitatively different in the near-surface region of the SrO-terminated STO crystal, possibly due to the presence of trapped charge on adsorbates bound to vacancy defects on the latter. The work function and electron affinity of MBE-grown SrTiO<sub>3-δ</sub>(001) on *p*-Ge(001) are very close to those of SrO-terminated bulk Nb:SrTiO<sub>3</sub>(001). However, the film surface most likely exhibits a mixed surface termination due to the formation of stacking faults resulting

from the symmetry mismatch with the substrate. The common work-function value for the bulk and heteroepitaxial film surfaces can be explained by the dominance of the SrO surface contribution for the latter; the secondary electron tail near the low-energy cutoff coming from the SrO-terminated portions of the surface overlaps and obscures the low-energy cutoff for the TiO<sub>2</sub>-terminated portions of the surface.

The work functions for the two ideal and defect-containing terminations were also calculated using *ab initio* DFT. Excellent agreement was found for the TiO<sub>2</sub>-terminated surface by assuming that the terminal plane is fully stoichiometric and essentially defect-free. Good agreement was also found for the SrO-terminated surface, but only for surfaces containing Sr and O vacancies bound to adsorbed O<sub>2</sub> and/or H<sub>2</sub>O from the vacuum environment of the MBE/XPS/UPS system which in turn trap itinerant electrons from donor dopants.

## ACKNOWLEDGMENTS

The authors are indebted to Dane Morgan and Ryan Jacobs for suggesting the problem, as well as for useful discussions. This work was supported by the U.S. Department of Energy, Office of Science, Division of Materials Sciences and Engineering under Award No. 10122 and was performed in the Environmental Molecular Sciences Laboratory, a national scientific user facility sponsored by the Department of Energy's Office of Biological and Environmental Research and located at Pacific Northwest National Laboratory.

- 
- [1] W. Meevasana, P. D. C. King, R. H. He, S. K. Mo, M. Hashimoto, A. Tamai, P. Songsiririthigul, F. Baumberger, and Z. X. Shen, *Nat. Mater.* **10**, 114 (2011).
- [2] A. F. Santander-Syro, O. Copie, T. Kondo, F. Fortuna, S. Pailhes, R. Weht, X. G. Qiu, F. Bertran, A. Nicolaou, A. Taleb-Ibrahimi, P. Le Fevre, G. Herranz, M. Bibes, N. Reyren, Y. Apertet, P. Lecoeur, A. Barthelemy, and M. J. Rozenberg, *Nature (London)* **469**, 189 (2011).
- [3] S. M. Walker, F. Y. Bruno, Z. Wang, A. de la Torre, S. Ricco, A. Tamai, T. K. Kim, M. Hoesch, M. Shi, M. S. Bahramy, P. D. C. King, and F. Baumberger, *Adv. Mater.* **27**, 3894 (2015).
- [4] M. Lorenz, M. S. R. Rao, T. Venkatesan, E. Fortunato, P. Barquinha, R. Branquinho, D. Salgueiro, R. Martins, E. Carlos, A. Liu, F. K. Shan, M. Grundmann, H. Boschker, J. Mukherjee, M. Priyadarshini, N. DasGupta, D. J. Rogers, F. H. Teherani, E. V. Sandana, P. Bove, K. Rietwyk, A. Zaban, A. Veziridis, A. Weidenkaff, M. Muralidhar, M. Murakami, S. Abel, J. Fompeyrine, J. Zuniga-Perez, R. Ramesh, N. A. Spaldin, S. Ostanin, V. Borisov, I. Mertig, V. Lazenka, G. Srinivasan, W. Prellier, M. Uchida, M. Kawasaki, R. Pentcheva, P. Gegenwart, F. M. Granozio, J. Fontcuberta, and N. Pryds, *J. Phys. D* **49**, 433001 (2016).
- [5] M. Coll, J. Fontcuberta, M. Althammer, M. Bibes, H. Boschker, A. Calleja, G. Cheng, M. Cuoco, R. Dittmann, B. Dkhil, I. El Baggari, M. Fanciulli, I. Fina, E. Fortunato, C. Frontera, S. Fujita, V. Garcia, S. T. B. Goennenwein, C. G. Granqvist, J. Grollier, R. Gross, A. Hagfeldt, G. Herranz, K. Hono, E. Houwman, M. Huijben, A. Kalaboukhov, D. J. Keeble, G. Koster, L. F. Kourkoutis, J. Levy, M. Lira-Cantu, J. L. MacManus-Driscoll, J. Mannhart, R. Martins, S. Menzel, T. Mikolajick, M. Napari, M. D. Nguyen, G. Niklasson, C. Paillard, S. Panigrahi, G. Rijnders, F. Sanchez, P. Sanchis, S. Sanna, D. G. Schlom, U. Schroeder, K. M. Shen, A. Siemon, M. Spreitzer, H. Sukegawa, R. Tamayo, J. van den Brink, N. Pryds, and F. M. Granozio, *Appl. Surf. Sci.* **482**, 1 (2019).
- [6] J. Hwang, Z. Feng, N. Charles, X. R. Wang, D. Lee, K. A. Stoerzinger, S. Muy, R. R. Rao, D. Lee, R. Jacobs, D. Morgan, and Y. Shao-Horn, *Mater. Today* **31**, 100 (2019).
- [7] A. Kahn, *Mater. Horiz.* **3**, 7 (2016).
- [8] R. Schlesinger, F. Bussolotti, J. P. Yang, S. Sadofev, A. Vollmer, S. Blumstengel, S. Kera, N. Ueno, and N. Koch, *Phys. Rev. Mater.* **3**, 074601 (2019).
- [9] R. Jacobs, J. Booske, and D. Morgan, *Adv. Funct. Mater.* **26**, 5471 (2016).
- [10] A. Ohtomo and H. Y. Hwang, *Nature (London)* **427**, 423 (2004).
- [11] S. Thiel, G. Hammerl, A. Schmehl, C. W. Schneider, and J. Mannhart, *Science* **313**, 1942 (2006).
- [12] N. Nakagawa, H. Y. Hwang, and D. A. Muller, *Nat. Mater.* **5**, 204 (2006).
- [13] M. Huijben, A. Brinkman, G. Koster, G. Rijnders, H. Hilgenkamp, and D. H. A. Blank, *Adv. Mater.* **21**, 1665 (2009).
- [14] J. Son, P. Moetakef, B. Jalan, O. Bierwagen, N. J. Wright, R. Engel-Herbert, and S. Stemmer, *Nat. Mater.* **9**, 482 (2010).

- [15] T. Susaki, A. Makishima, and H. Hosono, *Phys. Rev. B* **83**, 115435 (2011).
- [16] T. Susaki, N. Shigaki, K. Matsuzaki, and H. Hosono, *Phys. Rev. B* **90**, 035453 (2014).
- [17] T. Susaki, A. Makishima, and H. Hosono, *Phys. Rev. B* **84**, 115456 (2011).
- [18] I. Sokolović, M. Schmid, U. Diebold, and M. Setvin, *Phys. Rev. Mater.* **3**, 034407 (2019).
- [19] F. Gelle, R. Chirita, D. Mertz, M. V. Rastei, A. Dinia, and S. Colis, *Surf. Sci.* **677**, 39 (2018).
- [20] Y. Du, P. V. Sushko, S. R. Spurgeon, M. E. Bowden, J. M. Ablett, T.-L. Lee, N. F. Quackenbush, J. C. Woicik, and S. A. Chambers, *Phys. Rev. Mater.* **2**, 094602 (2018).
- [21] G. Kresse and J. Hafner, *Phys. Rev. B* **49**, 14251 (1994).
- [22] G. Kresse and J. Furthmüller, *Phys. Rev. B* **54**, 11169 (1996).
- [23] P. E. Blochl, *Phys. Rev. B* **50**, 17953 (1994).
- [24] S. L. Dudarev, G. A. Botton, S. Y. Savrasov, C. J. Humphreys, and A. P. Sutton, *Phys. Rev. B* **57**, 1505 (1998).
- [25] C. S. Fadley, *Prog. Surf. Sci.* **16**, 275 (1984).
- [26] W. F. Egelhoff, *Crit. Rev. Solid State Mater. Sci.* **16**, 213 (1990).
- [27] S. A. Chambers, *Adv. Phys.* **40**, 357 (1991).
- [28] C. S. Fadley, in *Synchrotron Radiation Research: Advances in Surface and Interface Science*, edited by R. Z. Bachrach (Plenum, New York, 1992), Vol. 1, p. 421.
- [29] P. S. Bagus, C. J. Nelin, C. R. Brundle, and S. A. Chambers, *J. Phys. Chem. C* **123**, 7705 (2019).
- [30] S. A. Chambers, M. H. Engelhard, L. Wang, T. C. Droubay, M. E. Bowden, M. J. Wahila, N. F. Quackenbush, L. F. J. Piper, T. L. Lee, C. J. Nelin, and P. S. Bagus, *Phys. Rev. B* **96**, 205143 (2017).
- [31] J. J. Yeh and I. Lindau, *At. Data Nucl. Data Tables* **32**, 1 (1985).
- [32] The  $\lambda$  values were determined by scaling the value measured for AlK $\alpha$ -excited valence band photoemission from thin epitaxial films of SrTiO<sub>3</sub> on Ge(001) by a factor of  $(E_k/1480)^{0.56}$ , where 1480 eV is the approximate kinetic energy of VB photoelectrons and  $E_k$  is the kinetic energy of either the Ti 2*p* or Sr 3*d* core levels. The 0.56 exponent in the power law comes from averaging over many materials within the region between  $E_k = 100$  and 1000 eV in Fig. 25 in S. Tanuma, C. J. Powell, and D. R. Penn, *Surf. Interface Anal.* **43**, 689 (2011). The  $\lambda$  value at  $E_k = 1480$  eV, and the way it was determined, can be found in Ref. [20].
- [33] S. Cook, K. Letchworth-Weaver, I.-C. Tung, T. K. Andersen, H. Hong, L. D. Marks, and D. D. Fong, *Sci. Adv.* **5**, eaav0764 (2019).
- [34] M. H. Hecht, *Phys. Rev. B* **43**, 12102 (1991).
- [35] M. S. J. Marshall, D. T. Newell, D. J. Payne, R. G. Egdell, and M. R. Castell, *Phys. Rev. B* **83**, 035410 (2011).
- [36] S. A. Chambers, Y. Du, Z. Zhu, J. Wang, M. J. Wahila, L. F. J. Piper, A. Prakash, J. Yue, B. Jalan, S. R. Spurgeon, D. M. Kepaptsoglou, Q. M. Ramasse, and P. V. Sushko, *Phys. Rev. B* **97**, 245204 (2018).
- [37] Z. Zhong and P. Hansmann, *Phys. Rev. B* **93**, 235116 (2016).
- [38] J. H. Haeni, C. D. Theis, and D. G. Schlom, *J. Electroceram.* **4**, 385 (2000).